A Scalable CMOS Molecular Electronics Chip for Single-Molecule Biosensing

Drew A. Hall, *Senior Member, IEEE*, Nagaraj Ananthapadmanabhan, Chulmin Choi, Le Zhang, Paul P. Pan, Christoph Von Jutrzenka, Thuan Nguyen, Jose Rizo, Macklan Weinstein, Raymond Lobaton, Prem Sinha, Trevor Sauerbrey, Cruz Sigala, Kathryne Bailey, Paul Mudondo, Ashesh Ray Chaudhuri, Simone Severi, Carl W. Fuller, James M. Tour, Sungho Jin, Paul W. Mola, and Barry Merriman

***Abstract*—This work reports the first CMOS molecular electronics chip. It is configured as a biosensor, where the primary sensor element is a single molecule "molecular wire" consisting of a ~100 GΩ, 25 nm long alpha-helical peptide integrated into a current monitoring circuit. The engineered peptide contains a central conjugation site for attachment of various probe molecules, such as DNA, proteins, enzymes, or antibodies, which programs the biosensor to detect interactions with a specific target molecule. The current through the molecular wire under a dc applied voltage is monitored with millisecond temporal resolution. The detected signals are ms-scale, picoampere current pulses generated by each transient probe-target molecular interaction. Implemented in a 0.18 µm CMOS technology, 16k pixel circuits are arrayed with a 20 µm pitch and read out at a 1 kHz frame rate. The resulting biosensor chip provides direct, real-time observation of the single-molecule interaction kinetics, unlike classical biosensors that measure ensemble averages of such events. This molecular electronics chip provides a platform for putting molecular biosensing "on-chip" to bring the power of semiconductor chips to diverse applications in biological research, diagnostics, sequencing, proteomics, drug discovery, and environmental monitoring.**

***Index Terms*—Single-molecule biosensor, molecular electronics, transimpedance amplifier, high-impedance sensor, biosensor.**

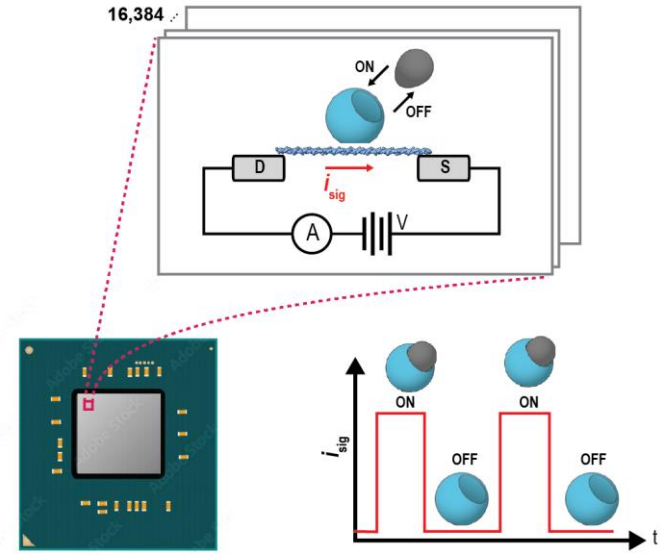

Fig. 1. Overview of a highly multiplexed, scalable CMOS-based molecular biosensor for single-molecule sensors.

I. Introduction

Molecular electronics is the concept of using single molecules as functional circuit elements. This concept was first put forth in the 1974 work of Aviram and Ratner [1], which envisioned special molecules to be used as rectifiers or switches. At the time, integrated circuits were rapidly shrinking following Moore's Law [2], and their work was motivated, in part, by considerations about the ultimate physical limits of circuit miniaturization. Then-recent discoveries in the 1960s that a single biomolecule, such as a cytochrome protein, could carry out complex electron transfer processes [3] also inspired their work. This was not long after Feynman's seminal 1959 proposal to extend engineering to the molecular scale [4]. While Feynman had, in effect, imagined nanotechnology as molecular mechanical engineering, the work of Aviram extended this to encompass molecular electrical engineering.

However, the visionary work of Aviram remained entirely theoretical for decades due to the inability to manipulate single molecules. This changed in 1998 when Tour and Reed [5] experimentally produced the first molecular electronic circuit by measuring the resistance of a single benzene molecule suspended between gold nanoelectrodes. At that time, the demonstration of the first molecular circuit was hailed as the scientific "Breakthrough of the Year" in Science [6], but the accompanying editorial noted that the real impact would come when molecular circuit elements could be integrated into CMOS chips.

In the present work, we introduce such a molecular electronics CMOS chip, realizing this nearly 50-year-long quest for molecular electronics – with the notable distinction that, instead of molecules being used as logic elements or memory

Manuscript received XXXXXXXXXXX; revised YYYYYYYYYY; accepted ZZZZZZZZZZ. This paper was approved by Associate Editor ABCD XYZAASDDDFSDF. This research is supported in part by the Office of the Director of National Intelligence (ODNI), Intelligence Advanced Research Projects Activity (IARPA), through Contract 2019-19081900003. (Corresponding Authors: Drew A. Hall and Barry Merriman)

The authors are with Roswell Biotechnologies, San Diego, CA 92121 USA (e-mail: barry.merriman@roswellbiotech.com).

Drew A. Hall is with the Department of Electrical and Computer Engineering, University of California, San Diego, La Jolla, CA 92093 USA (e-mail: drewhall@ucsd.edu).

Color versions of one or more figures in this paper are available online at http://ieeexplore.ieee.org.

Digital Object Identifier 12.3456/TBIOCAS.2022.0987654

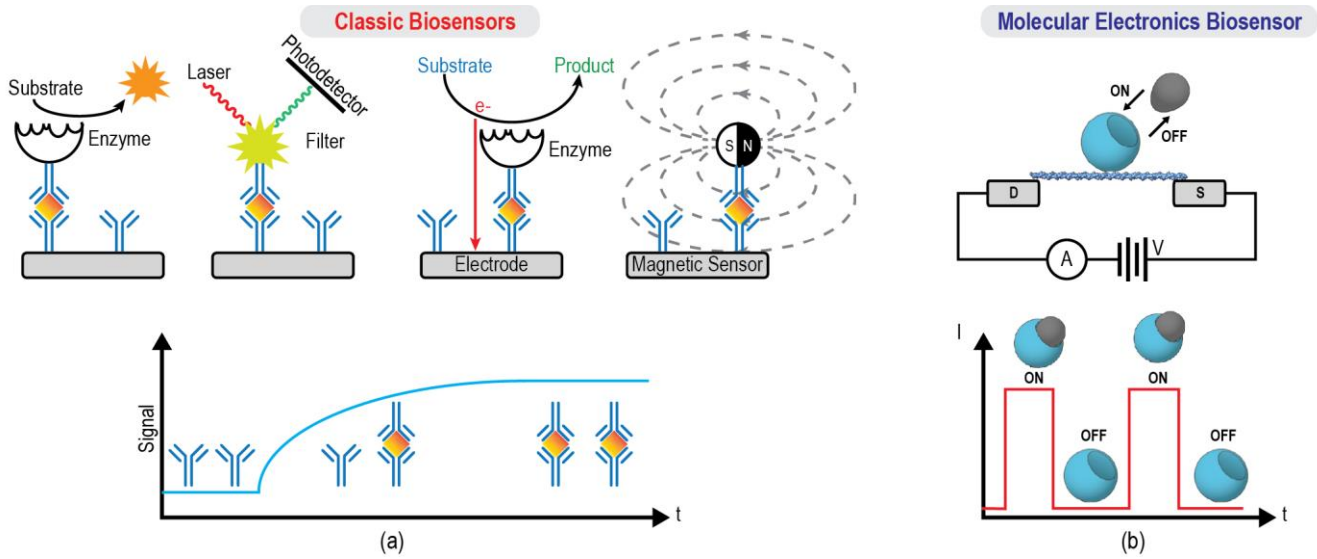

Fig. 2. (a) Overview of classical biosensors; (b) Molecular electronic single-molecule biosensor.

bits, as envisioned by the pioneers of the field, we propose that using single molecules as sensor elements is the "killer application" for molecular electronics. This is because silicon is exceptionally well-suited for logic and memory devices, as evidenced by nearly 60 years of Moore's Law scaling [7]–[9], while silicon has limited intrinsic sensing abilities, especially for biosensing [10], [11]. The primary motivation for a molecular electronics solution to sensing is to fundamentally solve the well-known "More-Than-Moore" scaling problem for sensors where transducer scaling is commonly the limiter to scaling chip-based sensor devices. Thus, the ideal solution is to have the transducer be a single molecule, which is already shrunk to the physical limit and will never inhibit future circuit scaling.

As shown in Fig. 1, the primary sensor element is a 25 nm long molecular wire connected to metal nanoelectrodes, which feed into a current monitoring circuit. The molecular wire contains a central conjugation site for attachment of various probe molecules (*e.g.*, DNA, proteins, enzymes, or antibodies) and is flanked by metal-binding domains for selective coupling to the nanoelectrodes. These current monitoring pixels are arrayed into a 16k sensor array that provides for control of the array and digital data readout at a 1 kHz frame rate. The molecular wires (and conjugated probes) are actively loaded into the circuit at startup using dielectrophoresis to trap molecules in the nanoelectrodes. Then, the current through the bridge molecule under a dc applied voltage is monitored with millisecond temporal resolution. The detected signals are ms-scale current pulses generated by each transient probe-target molecular interaction. This provides direct, real-time detection of the single-molecule interaction kinetics, in contrast to classical biosensors that often rely on indirect reporter mechanisms and measure ensemble averages of such events across many molecules and long times. This paper extends the work presented in [12], [13].

The remainder of this paper is organized as follows: Section II explains the sensor concept and contrasts single-molecule sensors with classical biosensors. Section III describes the chip architecture, and Section IV details the circuit implementation. Sensor post-processing is covered in Section V, and Section VI reports electrical and *in-vitro* measurement results. Finally, concluding remarks are made in Section VII.

II. Single-Molecule Biosensing

A common problem in biosensing is to detect a specific target biomolecule in a sample and, most ideally, to provide a quantitative measure of the target molecule concentration. Physical methods such as mass spectrometry, infrared spectrometry, and other forms of spectroscopy identify target molecules based on their physical properties, such as charge, mass, or interactions with photons [14]–[16]. However, these approaches typically cannot easily identify specific, complex biomolecules such as proteins, DNA segments, and diverse biochemicals, particularly in complex backgrounds of other such molecules, as is common for un-purified biological samples [17].

Such target biomolecules in complex backgrounds are instead resolved by relying on a specific binding probe molecule that selectively and specifically binds to the target molecule [18]. Common binding pairs that can form a probe and target include antibody-antigen pairs, a single-stranded DNA (ssDNA) and its complementary strand, a receptor protein and a ligand, or a synthetic DNA aptamer and its target molecule. Given a specific binding pair, such as an antibody-antigen, in a classical biosensor concept, such as those shown in Fig. 2(a), many probe molecules are attached to a solid support. When exposed to a sample, some target molecules present in the sample are bound and detected either through the presence of a reporter label (such as a fluorescent dye attached to the target) or a reporter mechanism that indirectly produces a localized detectable label (such as a secondary antibody with a dye label or linked to an enzyme that catalyzes an observable reaction, as in ELISA). Many such "labeled" biosensing schemes have been reported with optical [19], enzymatic [20], electrochemical

[21]–[27], and magnetic [28]–[30] reporters, among others. Label-free approaches have also been developed where the binding event changes a measurable physical property of the surface, such as the reflectance, plasmon resonance, or charge [31]–[34]. The temporal trajectory of such a reaction, if it were observed, would typically be a curve that picks up rapidly after the introduction of the analyte and saturates at some endpoint, as indicated in Fig. 2(a), representing the bulk, equilibrium kinetics of the binding interaction and reporter mechanism. In practice, the measurement is often performed at the endpoint, such as reading out the final equilibrium amount of fluorescence from a reporter dye.

In contrast to these classical biosensors, the single-molecule binding sensor reported here, see Fig. 2(b), measures the current versus time in real-time, passing through the molecular wire under an applied dc voltage. In this system, the individual molecular probe-target binding events change the impedance of the complex, and it is important to recall that these molecular binding events are commonly reversible. Hence, the actual bound state only exists *transiently* for some stochastic dwell time, and the probe will dynamically bind and unbind with target molecules in solution. As shown in Fig. 2(b), the ideal readout is a series of current pulses, each representing the direct observation of a single-molecule binding event. The duration of any given binding event is a stochastic random variable, sampled from the Boltzmann Distribution of statistical mechanics, which in turn depends on the binding energy and temperature. The waiting time between binding events is also a random variable, ideally exponentially distributed, where the mean waiting time is inversely related to the concentration of the target molecule. Thus, the mean waiting time provides a quantitative measure of the target concentration. One convenient expression for such a measure is the total fraction of time the sensor is in the bound state, which ideally obeys the classical first-order Michaelis-Menten rate law as a function of the target concentration [35].

Early scientific studies of electronic detection of single-molecule binding were done by non-specifically attaching single probe molecules on long carbon nanotubes and monitoring the nanotube current [36]–[38]. For the class of biosensors presented here to be both high performance and commercially viable, the design goal for the molecular component is precision at the nanoscale and manufacturability – that is, to have precision-engineered molecular constructs with precisely defined probe conjugation sites and end groups for nanoelectrode attachment, and that can be mass-produced by existing industrial means. Suitable molecular wires that fit these constraints include protein alpha-helical peptides or double-stranded DNA (dsDNA). The present work uses the peptide format as they have higher conductivity and are easier to synthesize with attachment points. The conductivity of peptide molecular wires and other proteins has recently been studied using sophisticated scanning probe techniques to directly measure the current passing through single protein molecules [39]–[42]. These molecular wires (or "bridge" molecules) have much lower conductivity than the carbon nanotubes; here, the nominal resistance is ~100 GΩ for the 25 nm long alpha-helical

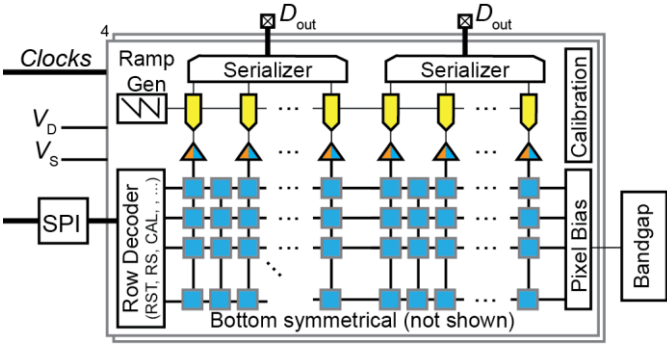

Fig. 3. System architecture.

peptide. These molecules may not have a net charge but are polarizable and thus can be electrically attracted to the nanoelectrodes by applying an ac voltage, a process known as dielectrophoresis (DEP) [43]. This active mechanism is used to rapidly load the molecules into the nanoelectrodes.

The signal generation mechanism in these sensors has not been fully characterized and remains largely an empirical observation. Multiple possible candidate modes for generating current modulation are evident, including field effects (from charges in the probe region modulating electron transport through the molecular wire), redox reactions, reconfigurations of the ion cloud around the molecules, and changes in the physical conduction paths available to charge transport electrons due to the probe-target interactions. For example, in the special case of Carbon Nanotube molecular wire sensors, an explicit field effect mechanism has been demonstrated to be the dominant signal generation mode [38], [44]. In part, this was demonstrated by increasing solution salt levels (decreasing the Debye shielding length) [44], which decreases the signal amplitude to near zero. Doing similar Debye shielding experiments for our sensors results in approximately 70% of the signal amplitude being eliminated at high salt, suggesting that field effects are a major component, but not the sole component, of the signal generation mechanism.

III. System Architecture

Small nanoelectrode test arrays were fabricated on a silicon substrate to understand the system requirements for the single-molecule biosensor. The discrete sensor devices were read out using a custom-designed front-end built using off-the-shelf components with support for up to 8 sensors. This system allowed rapid design exploration, such as trying different sensor geometries, electrode materials, applied bias voltage, and bridge molecules. After significant experimentation using this system, we found that for peptide-based bridges, the current ranged from 0.1 to 100 pA with a 0.5 V bias (V_{DS}) and a sampling rate of 1 kSps was sufficient to capture most interaction events. These specifications were then used to architect a scalable, high-density CMOS front-end with integrated sensors.

As shown in Fig. 3, this chip is arranged like a CMOS image sensor with a 2D pixel matrix divided into 4 sub-arrays, each containing 4,096 (64×64) pixels for a total array of 16,384

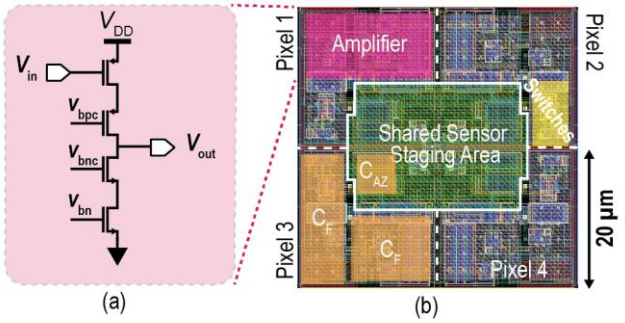

Fig. 4. a) Schematic of the pixel amplifier and b) annotated layout of a 2×2 grid of pixels.

pixels. This number of pixels supports multiplexing with redundancy and also reduces the assay response time. Each pixel contains a transimpedance amplifier, a column driver, and an electrode pair exposed to the solution for the bridge molecule to attach. The pixel area is limited to 20×20 µm^2, a constraint driven by the desire to have a full reticle chip with 1.5 million sensors. Each pixel must consume less than 2.5 µW to keep the surface heating less than 5 °C inside the flow cell with static fluid at the million-pixel scale. The top two rows of each sub-array are "dark" pixels where the electrodes are covered with oxide and thus not exposed to the solution as a negative control.

The sensor array is typically operated in a rolling shutter mode (*i.e.*, rows are sequentially reset with staggered read times). The reset can also be overridden through a global reset. A shift-register-based row decoder supplies the pixel control signals (*e.g.*, reset, mode, calibration, gain, etc.) and chooses a row of sensors to be read out. The shift register-based decoder avoids spurious glitches from a traditional decoder and allows for an arbitrary number of rows, whereas a decoder is limited to a power of 2. These digital signals are re-buffered between each sub-array by repeater cells. The selected row of pixels is read out by column-parallel ADCs butterflied along the top and bottom of the array. The top ADCs read pixels in the odd columns of the array, whereas pixels in even columns are read by the bottom ADCs. This split strategy allows the ADC to have twice the pixel pitch (*i.e.*, 40 µm). All other circuits (*e.g.*, row decoder unit cell, ADC, pixel bias, repeaters, etc.) are pitch-matched to the pixel (20 µm) to facilitate assembly.

The ADC outputs are aggregated by serializers into 16 lanes and captured using an FPGA. The FPGA also provides all clock and control signals to the chip and configures the chip through a serial peripheral interface (SPI). The sensor bias voltages, V_S and V_D, are provided from off-chip for maximum flexibility.

IV. Circuit Implementation

A. Auto-zeroed Transimpedance Amplifier

The core of the pixel is a capacitive transimpedance amplifier (C-TIA) that integrates the pA-level sensor current on a feedback capacitor, C_F. The amplifier is implemented with a single-ended, common-source amplifier, as shown in Fig. 4(a). The input device is a 3 V I/O PMOS transistor for lower flicker (1/*f*) noise and cascoded with core devices for high output impedance. The pixel supply voltage is 2.1 V, allowing for a high output swing.

The amplifier was sized to have a dc gain of 70 dB and a 7 MHz open-loop unity-gain bandwidth with a 1 µA bias current. Due to the limited area (400 µm^2), it was impossible to size the transistors large enough to have a low flicker (1/*f*) noise corner. Instead, this was mitigated actively through auto-zeroing, which also samples the correct bias voltage. With the post-processing scheme described later, most of the top metal is needed for the sensor staging area. Unfortunately, in this process, the top metal is required to contact the metal-insulator-metal (MIM) capacitors. Thus, the feedback capacitors were implemented using all the available MIM area since they need to be very linear, and the auto-zero capacitor, C_{AZ}, was implemented using a MOSFET capacitor underneath the staging area, as shown in Fig. 4(b). To create a larger window for post-processing, the pixels are arranged in a 2×2 grid with mirroring and flipping to group the sensor openings. This larger window is needed during the sacrificial etch process described later. Single vias to the top metal will eventually become nanoelectrodes. These are all shorted together during fabrication by the top metal covering the staging area. This also provides ESD protection from the source-side connection.

Ideally, one would route currents to the pixels and locally generate the necessary bias voltages to minimize coupling and the effect of mismatch, but there is insufficient reaming area at the desired pixel pitch. Instead, the bias generation is shared by all pixels in a row. Row level (vs. column or another arrangement) was chosen since the pixels are all reset simultaneously, thus correlating the bias disturbance. An on-chip bandgap reference generates a supply- and temperature-insensitive current that is then mirrored to 256× replica bias circuits (one per row per sub-array). The repeater cells that buffer the digital signals also incorporate decoupling capacitors for the analog bias signals.

The pixel operation, shown in Fig. 5, is as follows: 1) During reset (RST), the capacitance at the virtual ground node is charged to V_D. A bias voltage, V_S, is constantly applied to the other side of the sensor. The amplifier is auto-zeroed at this time to remove its 1/*f* noise and set the bias by sampling these on C_{AZ} = 75 fF. 2) During the integration phase, the sensor current is integrated on a 1-bit selectable feedback capacitor, C_F = 200 fF (150 pA dynamic range) or 400 fF (300 pA dynamic range). Normal operation ping-pongs between reset (15.625 µs) and integration (984.375 µs). At startup, a switch (MODE) removes the sensor from the circuit, and a calibration current is applied to verify the pixel functionality. The calibration current is supplied from off-chip, attenuated, and copied to each column using a cascoded current mirror. All switches connected to the sensitive virtual ground node are low-leakage T-switches [22], where the internal switch node is driven to V_D to minimize the voltage drop across the switch in the off-state.

B. Split Buffer Column Driver

The C-TIA drives a split buffer, half of which is inside the pixel, with the rest shared by all pixels in the column, as shown in Fig. 6. This architecture was chosen over a conventional

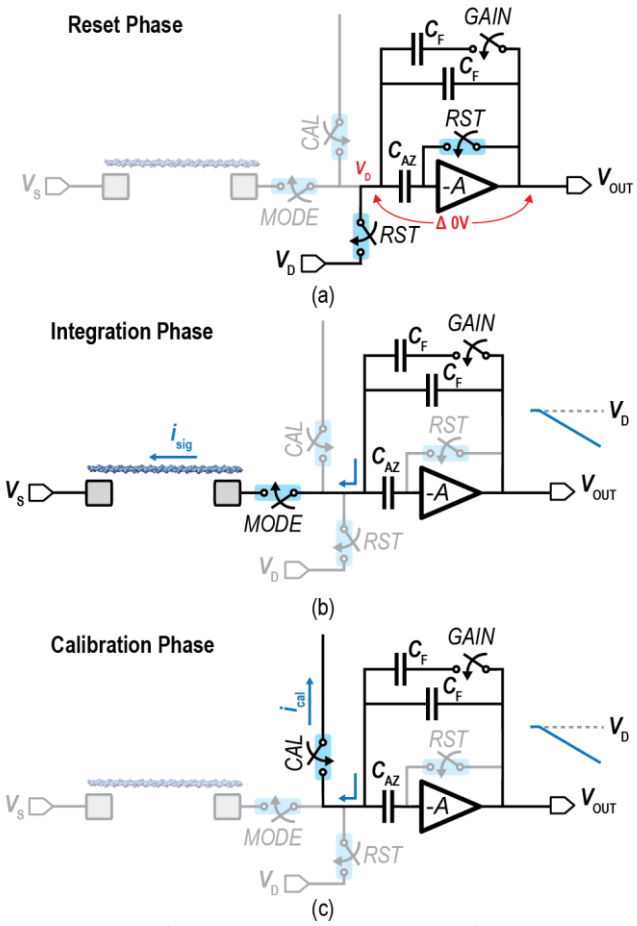

Fig. 5. Schematic of auto-zeroed transimpedance amplifier during the (a) reset, (b) integration, and (c) calibration phases.

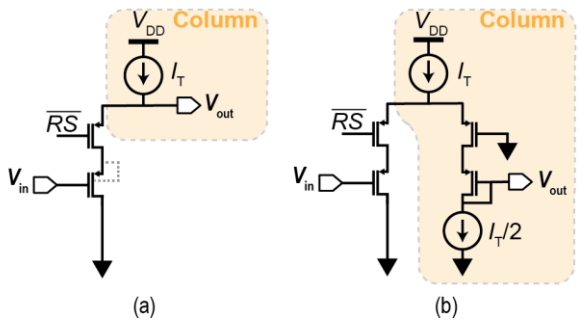

Fig. 6. Schematics of a (a) conventional source follower with optional body tie and (b) split-buffer amplifier.

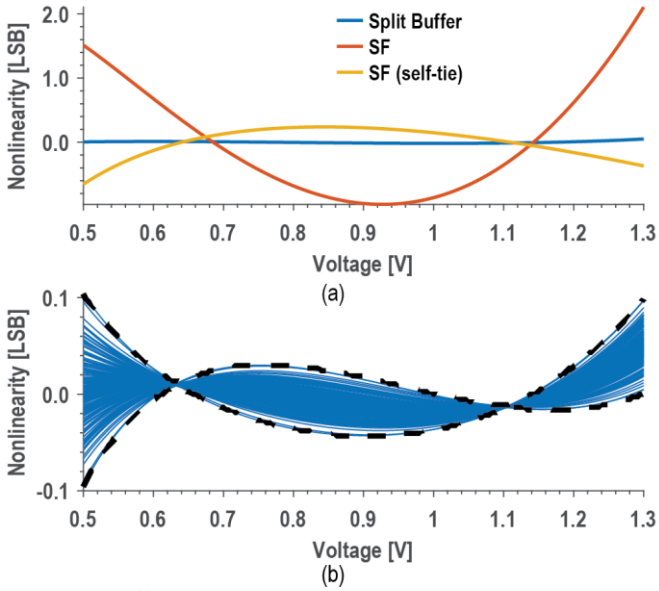

Fig. 7. Split buffer simulations showing (a) nonlinearity and (b) Monte Carlo variation (n = 100).

source follower-based column driver because it has higher linearity and is inherently a current-mode circuit with low impedance nodes for fast settling when switching rows. Even when the bulk of the source follower is tied to the source, the simulated source follower-based buffer nonlinearity is worse than the split buffer, as shown in Fig. 7(a). The split buffer does not need the body-source tie, simplifying the layout since all the PMOS devices can share a common n-well. The better linearity stems from the partial cancellation of nonlinearities due to the differential nature of the circuit. A Monte Carlo simulation with 100 runs was performed to demonstrate the circuit's robustness. As shown in Fig. 7(b), the worst-case nonlinearity is less than 0.2 LSBs across the entire voltage range.

With a 1,000 frame/s sampling rate, the ADC has 15.625 µs for settling (2.825 µs) and conversion (12.8 µs). In both column driver approaches, there is a significant capacitance hanging on the output node consisting of the routing and the column drivers of all the off rows. This capacitance is 660 fF based on post-layout extraction. The buffer was designed to settle in less than 1.25 µs. Another benefit of the split-buffer structure is that it allows for level-shifting such that the ADCs can operate from a nominal 1.8 V supply voltage.

C. *Column-Parallel Single-Slope ADC*

The 64 kSps ADCs are implemented using a single-slope architecture with two preamplifiers, a strong-arm latch, and an 11-bit counter, as shown in Fig. 8(a). The counter has an additional bit (not read out) to catch overflow without wrapping. Two preamps were used to suppress the latch's offset and minimize comparator kickback on the shared ramp signal. Each open-loop preamplifier consumes 28 µW and has a 100 MHz unity-gain bandwidth with 20 dB dc gain. The simulated input-referred noise of the amplifier is 74 μV_{rms}. Like the pixel, the preamplifier bias is shared by all ADCs in a sub-array.

The shared ramp generator (one per side of each sub-array) is realized by an integrator with a programmable current source, as shown in Fig. 8(b). This amplifier-based feedback structure maintains the voltage across the current source (to maximize the linearity) while also providing a low output impedance to drive the preamplifiers. The ADC is reconfigurable between 8- and 10-bit modes by changing the clock. The integration current is digitally programmable via the SPI bus in 30 nA steps with a nominal 5 µA current. The current is integrated on a 12.8 pF MIM capacitor. The amplifier is implemented with a single-stage folded-cascode structure with a dc gain of 84 dB and a 35 MHz unity-gain bandwidth.

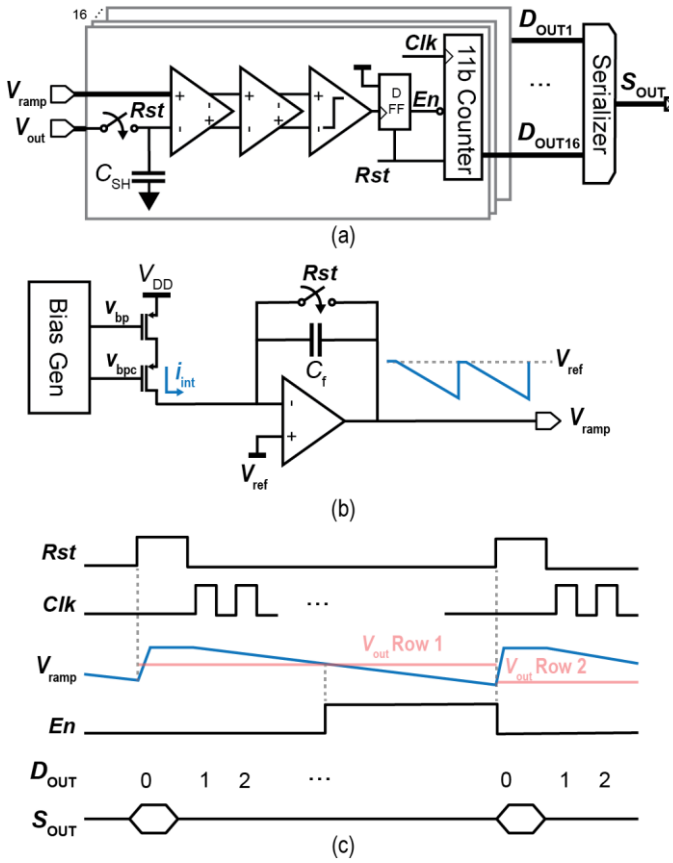

Fig. 8. Schematics of the (a) column-parallel single-slope ADC, (b) ramp generator, and (c) timing diagram.

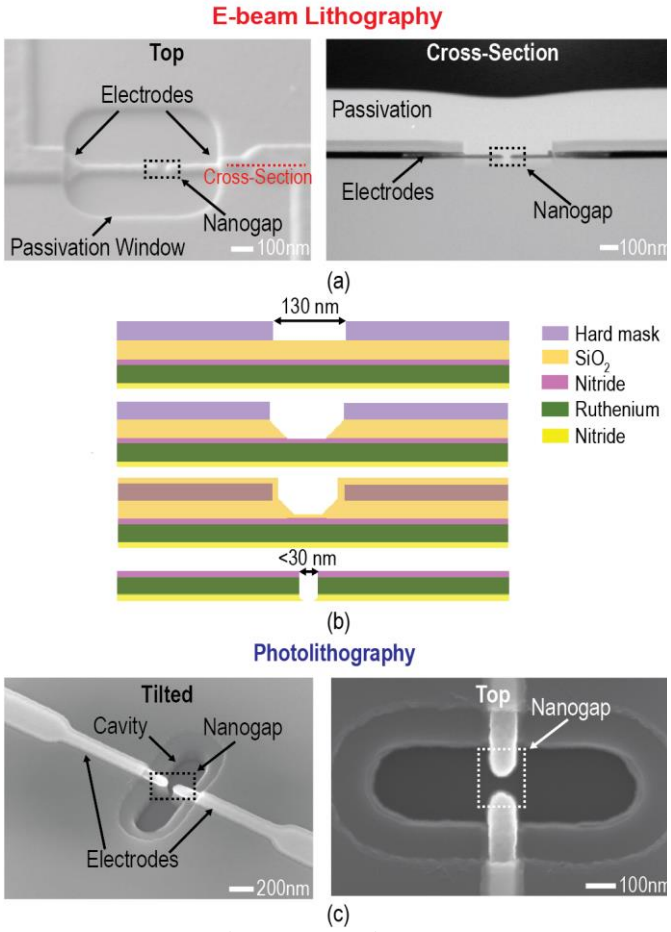

Fig. 9. (a) SEM images of nanoelectrodes fabricated via E-Beam lithothography. (b) Photolithography gap narrowing process and (c) SEM images of fabricated nanoelectrodes.

Fig. 8(c) shows a timing diagram for each conversion. First, the voltage from the split buffer is sampled onto a capacitor. Simultaneously, the ramp generator, sparkle latch, and counter are reset. The ADC clock is gated by the reset signal and held low. Once the reset signal is de-asserted, the ramp generator starts integrating the current ramping down from the full-scale voltage towards zero. The counter increments each ADC clock cycle until the ramp signal crosses the value stored on the sample and hold capacitor, C_{SH}, after which a sparkle latch (a D flip-flop) captures the comparator output to prevent retriggering, and the counter stops incrementing. The ADC outputs are aggregated by a shift register-based serializer running at 11 Mbps with 16 lanes and captured using an off-chip FPGA. The data is shifted off during the reset period to minimize coupling.

V. Post-Processing

The precision-engineered molecular wires, such as dsDNA or the present helical peptides, are by design at the nanometer scale (<30 nm), thus requiring the gap between the electrodes to be smaller than what is possible in standard CMOS back end of the line (BEOL) metallization. Furthermore, the electrodes must be electrochemically stable in ionic solutions, precluding the use of standard metals like copper and aluminum. After a detailed material compatibility study, ruthenium (Ru) was chosen due to its foundry compatibility, robustness, and electrochemical performance. Two approaches were developed to pattern the nanoelectrodes, electron-beam lithography (EBL) (ideal for agile R&D) and conventional photolithography (ideal for mass production at CMOS foundries).

A. *Electron-Beam Lithography*

For EBL nanoelectrodes, the wafer is spin-coated with photoresist (NR9-6000PY) and patterned to selectively etch the sacrificial 23×15 μm^2 "bond pads" over the sensor vias using Aluminum Etchant Type A (Transene). This process leaves the outer real bond pads intact while exposing the tungsten vias in the common staging area for the electrodes of 4 adjacent pixels. This sacrificial approach is necessary as the top metal is too rough to pattern nanoelectrodes directly. The metal 5-6 vias are the last planarized layer in the commercial foundry's fabrication process ensuring planarity. Next, the nanoelectrodes are written by spin coating polymethyl methacrylate (PMMA) A2 and patterning it using a Vistec EBPG 5200 (4 nm beam radius, 30 keV accelerating voltage, and 10 pA beam current). This results in 50 nm wide electrodes with less than 20 nm gaps. A 5 nm chromium (Cr) and 20 nm ruthenium (Ru) film stack is deposited and subsequently lifted off. A second EBL process places a 5 nm Cr, 50 nm Ru, and 50 nm hafnium oxide (HfO) film stack to cap the vias and cover part of the wire with oxide to minimize current leakage into the electrolyte. Fig. 9(a) shows

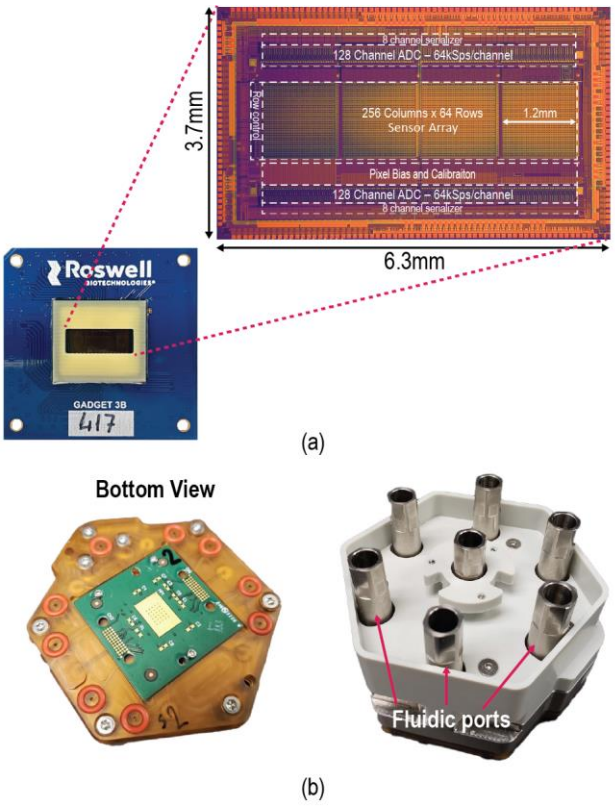

Fig. 10. (a) Annotated die micrograph on a "chip-on-board" package and (b) photograph of the backside of packaged chip (left) and assembled flowcell (right).

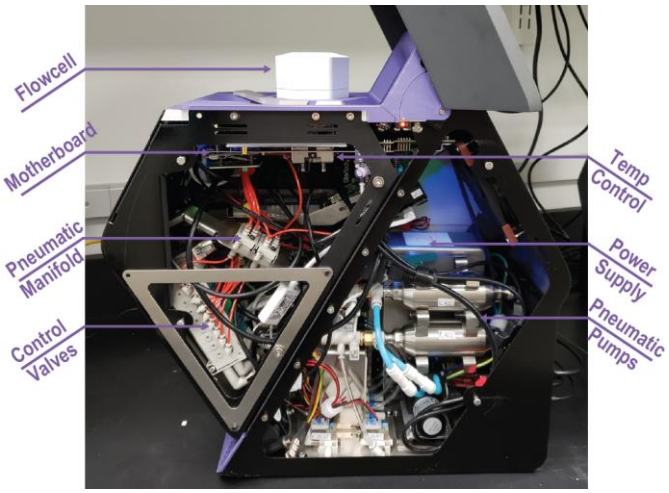

Fig. 11. Annotated photograph of instrument.

a representative nanoelectrode visualized using a Zeiss Sigma 500 emission scanning electron microscope (SEM) and a cross-section of the nanoelectrode.

B. Photolithography

For conventional photolithography, the wafers are pulled before passivation with individual top metal pads for each electrode (instead of the sacrificial bond pad used for EBL). Tungsten vias and oxide are subsequently added and planarized. A blanket 3 nm tantalum nitride (TaN), 15 nm Ru, and 3 nm titanium nitride (TiN) film stack is deposited, followed by a 50 nm SiO_2 layer deposited with plasma-enhanced chemical vapor deposition (PECVD). A deep-ultraviolet (DUV) resist is coated on the SiO_2 layer to define the nanoelectrode using a gap narrowing technique. After light-field exposure using 193 nm immersion lithography, the resist is developed, and the unprotected oxide is removed via RIE etching. A hard mask is deposited on the remaining SiO_2 structure, and a dark-field exposure is used to print a 150 nm gap into the SiO_2. A proprietary etch chemistry results in a tapered etch profile and achieve a final distance of 50 nm between the bottoms of the SiO_2 mandrels. To reduce the electrode gap, spacer patterning is employed. Highly conformal SiO_2 is deposited via plasma-enhanced atomic layer deposition (PEALD) atop the SiO_2 mandrels, as shown in Fig. 9(b). The resulting <30 nm gap is transferred into the metal layers by ion-beam etching through the underlying SiO_2 matrix. To protect the vias, 20 nm SiO_2 and 30 nm SiN are deposited by PECVD. Passivation over the bond pads is removed by a photolithographically enabled oxide etch landing on the bond pad layer. To open the nanoelectrode area, a DUV resist is spin-coated as an etch mask for a cavity (800 × 800 nm^2). After exposure, the resist is developed, and the passivation dielectric layers are etched using IBE. Fig. 9(c) shows SEM images of the resulting nanoelectrodes. Direct patterning of the nanoelectrodes is impossible using the current 200 mm tool line. This process is foundry compatible and capable of producing nanoelectrodes at scale.

VI. Measurement Results

This chip was fabricated in a 180 nm CMOS process with a multilayer mask (MLM). Wafers were post-processed to fabricate nanoelectrodes with a range of gaps (10-12 nm, 14-16 nm, 17-20 nm, and 20-30 nm) using EBL and photolithography. The chips were wire-bonded directly to a printed circuit board (PCB) with partial encapsulation to expose the pixel array, as shown in Fig. 10(a), and mounted in a custom flow cell with a platinum rooftop pseudo-reference electrode and fluidic access ports [see Fig. 10(b)]. The pseudo-reference electrode sets the bulk solution potential and is driven by a low-impedance source rather than a potentiostat.

A. Instrument

The chip cartridge plugs into an instrument that controls reagent delivery and handles all electrical signals. Fig. 11 shows a photograph of the instrument containing the microfluidic flow cell, motherboard, temperature controller, power supply, and pneumatic control for reagent delivery. The motherboard has an FPGA (Opal Kelly XEM6310), an ac waveform generator for dielectrophoresis, and an SPI bus for monitoring the chip's critical currents, voltages, and temperatures. The FPGA acquires the ADC data (at 20 MB/s), buffers it, and sends it to a computer via USB, where it is streamed to a solid-state disk. The data is subsequently transposed offline to ease time series analysis and stored in HD5 files. The sample being tested is loaded into the top of the cartridge, whereas all other reagents are stored on the instrument and delivered to the chip through pneumatic control in a software-programmable sequence.

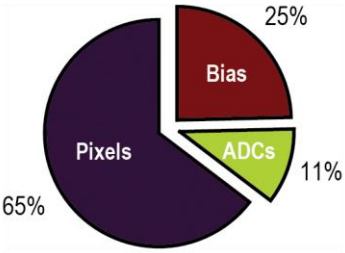

Fig. 12. Measured power consumption.

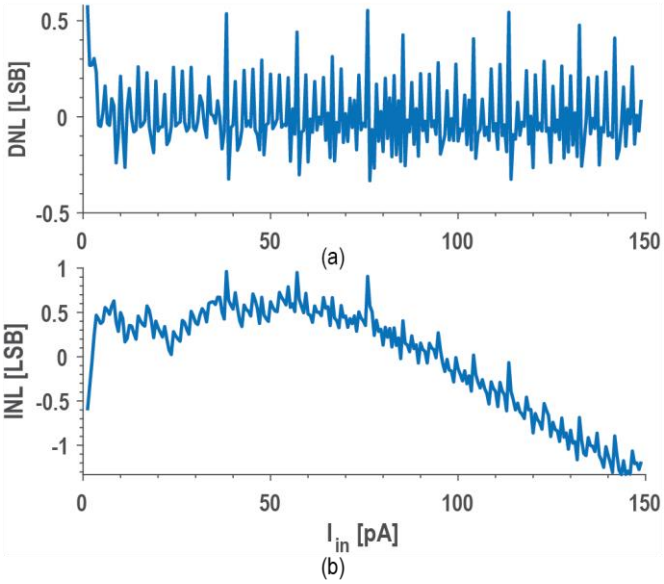

Fig. 13. Measured signal path (a) DNL and (b) INL.

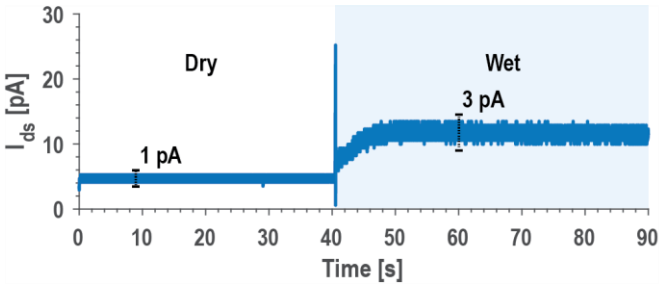

Fig. 14. Measured leakage (a) dry and (b) wet.

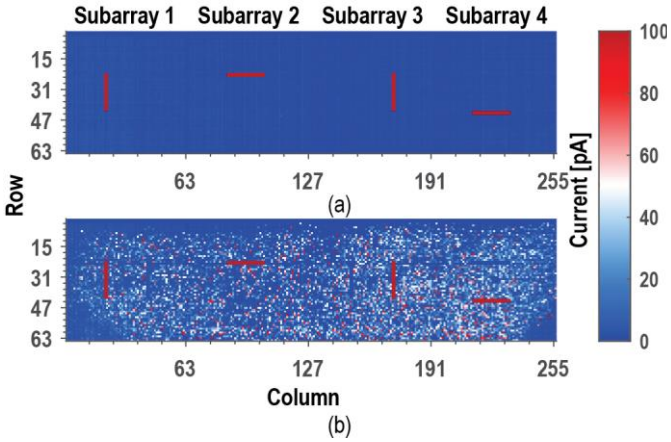

Fig. 15. Measured signal across array at the (a) start of the experiment prior to loading the bridges and (b) after the assay completion.

B. *Electrical Characterization*

The chip operates off a 2.1 V supply for the pixels and buffer and 1.8 V for the remaining circuits, consuming 58 mW, as shown in Fig. 12. Most of the power is dissipated in the pixels (37.8 mW) followed by the ADCs (14.4 mW). The measured input-referred integrated noise is 39 fA_{rms} for C_F = 200 fF and 76 fA_{rms} for C_F = 400 fF. Fig.13 shows the measured signal path (pixel and ADC) linearity acquired by sweeping the calibration current across the input range. The average differential nonlinearity (DNL) is +1.5/-0.7 LSB, and the integrated nonlinearity (INL) is ±2 LSB. The measured residual input-referred offset is 2.5-5 pA across the array due to the buffer and ADC preamplifier offsets, which are not auto-zeroed. The measured leakage current fluctuates by <1 pA dry and 3 pA in distilled water, with minimal dependence on V_{DS} (nominally V_D = 1.3 V and V_S = 0.8 V), as shown in Fig. 14. The digital signal integrity was measured using a Keysight Infinium oscilloscope. When shifting the data off of the chip at 80 MHz, the eye had an opening of 9.7 ns and 1.3 V. Finally, Fig. 15 shows an illustrative example of the entire array being read out before and while an assay was run. The red lines in Fig. 15(a) are control pixels where the nanogap is intentionally shorted to debug sensor failures. Fig. 15(b) shows a snapshot of the array during an assay where the pixels' real-time activity is observed.

C. *in-vitro Characterization*

The bridge molecules must be loaded into the circuit for use as a sensor. Delivery by passive diffusion alone can require over 24 hours, even at a high concentration. Instead, the much faster process of active dielectrophoretic trapping is employed by applying an ac voltage to the electrodes for 10-second intervals, as shown in Fig. 16. The "boot up" phase consists of up to 10 rounds of such active bridging, applying a 1.6 V_{pp} sinusoid at 100 kHz through V_S with V_D held at a fixed potential (by keeping the amplifier in reset). During the bridging phase, the buffer is a low ionic strength solution to prevent Debye screening. After each DEP round, the array is read out to determine if a bridge was incorporated, as observed by an increase in the pixel current. A pixel is marked as bridged if two successive measurements show an elevated current, and trapping is stopped to prevent additional bridging. An exemplar SEM image of a single "dumbbell" bridge (made observable by the addition of two 10 nm diameter gold beads capping a 25 nm dsDNA molecular wire) spanning the electrode gap is shown in Fig. 16(b). In theory, multiple bridges could bind to a sensor. This is controlled by limiting the number of DEP rounds and observing the sensors after each round of bridging.

Orthogonal (non-electrical) verification of a single bridge molecule in the circuit is challenging due to their nanometer dimensions and low contrast. Platinum nanoparticles (d = 30 nm) can be trapped in the gap and easily imaged with SEM, as shown in Fig. 17(a); however, similar direct imaging of peptide or dsDNA bridges is impossible. Instead, one must either label the bridge with metal nanoparticles for SEM imaging, or

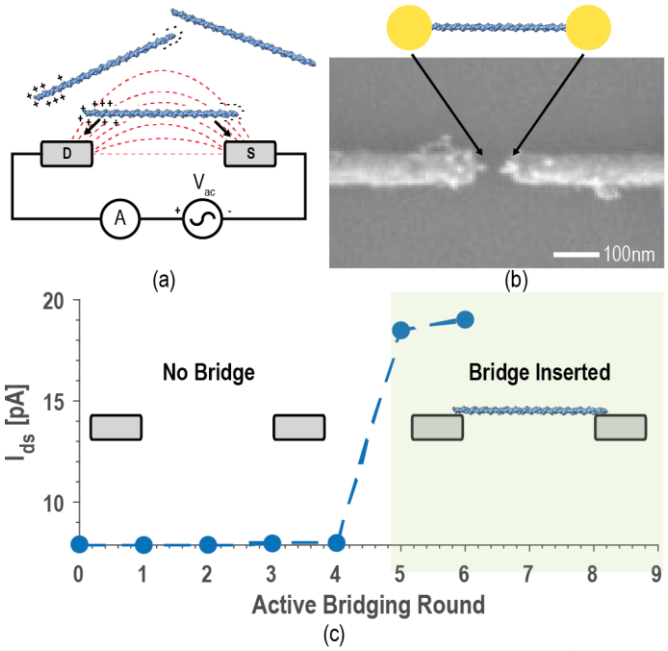

Fig. 16. (a) Dielectrophoretic trapping concept, (b) SEM image of dsDNA with gold beads, and (c) measured current after successive active bridging rounds, resulting in bridging.

measure the nm changes in *z*-height with atomic force microscopy (AFM). Fig. 17(b) shows an AFM image of a nanoelectrode with a single bridge molecule. This process is slow and limited in the scanning area and is only used as a proof-of-concept verification rather than for routine systematic assessments.

To show this platform's versatility, we demonstrate a model "diagnostic" assay, specifically a protein binding or "antigen" test. The probe on the peptide bridge is a DNA aptamer (about 100 nt in length) having an affinity for his-tagged proteins with a K_d of approximately 1-3 pM [45]. The target protein is a fragment of the Spike (or S-) protein from the surface of the COVID-19 virus made with an N-terminal his-tag. The scheme is shown in Fig. 18(a), where the aptamer is attached to the bridge using a "click" chemistry linker [13]. In the presence of the RBD protein, the sensor current exhibits pulses corresponding to individual aptamer-protein binding events, as shown in Fig. 18(b). As expected, the rate of pulse detection (and the fraction of time in the bound state) increases with higher target molecule concentration, while the pulse widths remain constant on average as they are governed only by the binding energy of the interaction. The bound/unbound states in the signal time traces were identified by analysis with a 3-state Hidden Markov Model (HMM) [46]. In these experiments, more than 1000 binding events are observed over each 3-minute period of target concentration exposure. Critically, the sensor output is flat in the absence of the RBD target molecule and in the presence of diverse off-target molecules, indicating that the sensor is highly specific, despite being extremely sensitive. Plotting the fraction of the time bound versus the target concentration, as shown in Fig. 18(c), produces a classical binding calibration curve of a Michaelis-Menten form. Using this, we find the COVID-19 antibody has a measured

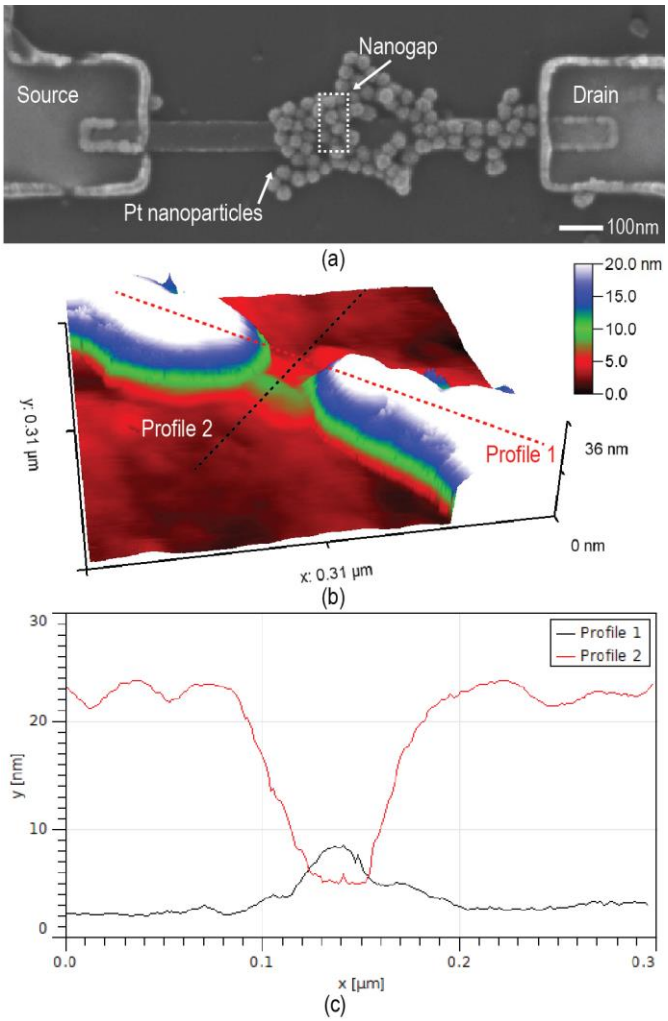

Fig. 17. (a) SEM images of platinum nanoparticles trapped between electrodes, (b) 3D AFM image of a bridge between electrodes, and (c) profile along the annotated lines.

disassociation constant, K_d, of 1.3 pM in phosphate-buffered saline (PBS). Finally, and critically important for real diagnostic applications, we found that this viral sensor can also work directly in physiological fluids by measuring similar concentration curves in pure PBS, 20% human plasma, and 100% artificial human plasma. Table I lists the fitted assay parameters, including the 95% confidence interval (CI), that are in close agreement regardless of the sample matrix and are similar to values reported in the literature for similar aptamers.

This is only one of the many possible assays that this platform supports. We have also shown that the probe molecule can be ssDNA, antibodies, aptamers, and enzymes [13]. Of particular interest is the case where the probe is a DNA polymerase enzyme, such as Phi29. When this sensor is primed ssDNA template and free nucleotides, the polymerase can be observed in real-time to copy the template, where the specific pulses represent individual nucleotide incorporation events. This sensor provides the basis for long-read, rapid sequencing of single DNA molecules by using the pulse features to accurately identify which pulses represent A, G, T, and C events. In this context, the extreme scalability of the CMOS

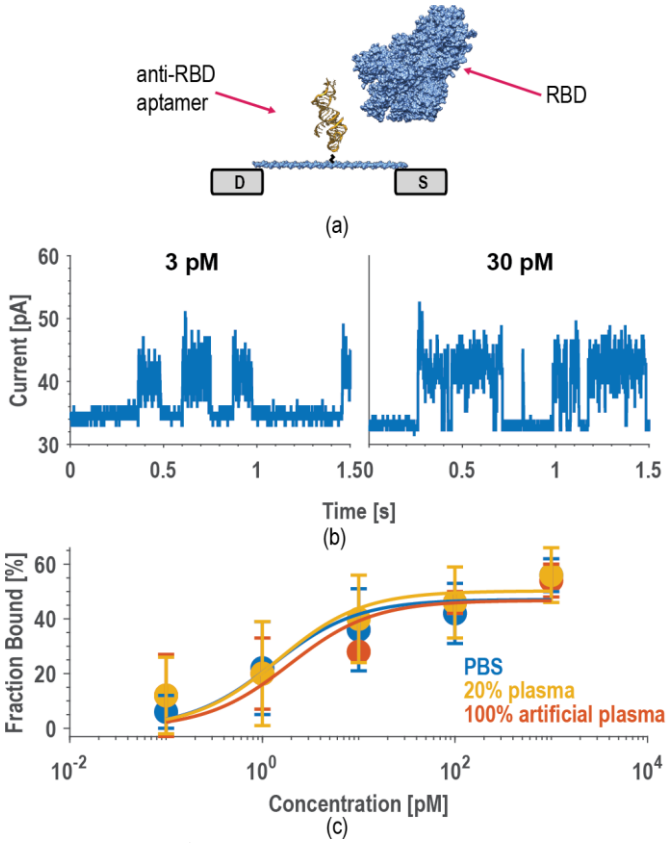

Fig. 18. (a) Scheme for COVID-19 his-tagged protein assay; (b) current vs. time trace at different concentrations; and (c) calibration curve showing fraction bound vs. concentration.

TABLE I
MEASURED ASSAY PARAMETERS

	PBS Buffer		20% Plasma		100% Artificial Plasma	
	Value	**95% CI**	**Value**	**95% CI**	**Value**	**95% CI**
B_{max}	0.47	0.4-0.55	0.47	0.39-0.58	0.5	0.41-0.6
K_d (pM)	1.3	0.4-4.5	1.9	0.39-11	1.5	0.35-5.7

molecular electronics chip offers the potential to dramatically reduce the time and cost of whole genome sequencing.

VII. Conclusion

This work reported the first CMOS molecular electronics chip, configured to be a programmable biosensor based on a molecular wire trapped between two nanoelectrodes of a current monitoring circuit. A 16k pixel CMOS chip was designed with a sub-pA sensitivity and 1,000 frame/s readout rate to monitor probe-target molecule interactions. Post-processing techniques were developed to scalably fabricate nanoelectrodes with sub-30 nm gaps using EBL and photolithography. Finally, we demonstrated the biosensor functionality with a model COVID-19 diagnostic assay performed in a complex physiological (plasma) sample.

This chip can also monitor single-molecule binding interactions for antibody-antigen and drug-receptor binding or for monitoring CRISPR/Cas enzyme activity. For such diverse biosensing applications, this platform provides the foundation for creating assays with high levels of multiplexing, rapid response on the scale of seconds, a limit-of-detection down to single molecules, and a dynamic range of pulse rate spanning many orders of magnitude, the simplicity of label-free detection, and deployable on low-cost CMOS chip and instruments that are well-suited to distributed applications. In summary, this work presents the first molecular electronics CMOS biosensor chip and demonstrates its broad utility for single-molecule sensing applications.

Acknowledgments

The authors would like to acknowledge the contributions of past and present employees of Roswell, whose collective efforts made this work possible, and Emad AlZaben, Sue Smalley, and Kevin Wall for their long-standing encouragement and support. We dedicate this work to the memory of Dr. Mark Reed, whose pioneering work, vision, and encouragement inspired many to work towards the goal of molecular electronics.

References

[1] A. Aviram and M. A. Ratner, "Molecular rectifiers," *Chem. Phys. Lett.*, vol. 29, no. 2, pp. 277–283, Nov. 1974.

[2] G. E. Moore, *Cramming more components onto integrated circuits*. McGraw-Hill New York, 1965.

[3] A. Kowalsky, "A Study of the Mechanism of Electron Transfer in Cytochrome c," *J. Biol. Chem.*, vol. 244, no. 24, pp. 6619–6625, Dec. 1969, doi: 10.1016/S0021-9258(18)63451-9.

[4] R. P. Feynman, "Plenty of Room at the Bottom," 1959.

[5] M. A. Reed, C. Zhou, C. J. Muller, T. P. Burgin, and J. M. Tour, "Conductance of a Molecular Junction," *Science*, vol. 278, no. 5336, pp. 262–254, Oct. 1997.

[6] R. F. Service, "Molecules Get Wired," *Science*, vol. 294, no. 5551, pp. 2442–2443, Dec. 2001, doi: 10.1126/science.294.5551.2442.

[7] M. Bohr, "A 30 Year Retrospective on Dennard's MOSFET Scaling Paper," *IEEE Solid-State Circuits Soc. Newsl.*, vol. 12, no. 1, pp. 11–13, 2007, doi: 10.1109/N-SSC.2007.4785534.

[8] M. Bohr, "The new era of scaling in an SoC world," in *2009 IEEE International Solid-State Circuits Conference - Digest of Technical Papers*, Feb. 2009, pp. 23–28. doi: 10.1109/ISSCC.2009.4977293.

[9] F. Schwierz and J. J. Liou, "Status and Future Prospects of CMOS Scaling and Moore's Law - A Personal Perspective," in *2020 IEEE Latin America Electron Devices Conference (LAEDC)*, Feb. 2020, pp. 1–4. doi: 10.1109/LAEDC49063.2020.9073539.

[10] S. Forouhi, R. Dehghani, and E. Ghafar-Zadeh, "CMOS based capacitive sensors for life science applications: A review," *Sens. Actuators Phys.*, vol. 297, p. 111531, Oct. 2019, doi: 10.1016/j.sna.2019.111531.

[11] A. Hassibi, N. Wood, and A. Manickam, "CMOS biochips: Challenges and opportunities," in *2018 IEEE Custom Integrated Circuits Conference (CICC)*, Apr. 2018, pp. 1–7. doi: 10.1109/CICC.2018.8357043.

[12] D. A. Hall *et al.*, "A CMOS Molecular Electronics Chip for Single-Molecule Biosensing," in *2022 IEEE International Solid- State Circuits Conference (ISSCC)*, Feb. 2022, vol. 65, pp. 1–3. doi: 10.1109/ISSCC42614.2022.9731770.

[13] C. W. Fuller *et al.*, "Molecular electronics sensors on a scalable semiconductor chip: A platform for single-molecule measurement of binding kinetics and enzyme activity," *Proc. Natl. Acad. Sci.*, vol. 119, no. 5, p. e2112812119, Feb. 2022, doi: 10.1073/pnas.2112812119.

[14] P. Singh, "SPR Biosensors: Historical Perspectives and Current Challenges," *Sens. Actuators B Chem.*, vol. 229, pp. 110–130, Jun. 2016, doi: 10.1016/j.snb.2016.01.118.

[15] Á. I. López-Lorente and B. Mizaikoff, "Mid-infrared spectroscopy for protein analysis: potential and challenges," *Anal. Bioanal. Chem.*, vol. 408, no. 11, pp. 2875–2889, Apr. 2016, doi: 10.1007/s00216-016-9375-5.

[16] "Beyond mass spectrometry, the next step in proteomics." https://www.science.org/doi/10.1126/sciadv.aax8978 (accessed Jul. 15, 2022).

[17] S. Alseekh *et al.*, "Mass spectrometry-based metabolomics: a guide for annotation, quantification and best reporting practices," *Nat. Methods*, vol. 18, no. 7, Art. no. 7, Jul. 2021, doi: 10.1038/s41592-021-01197-1.

[18] "The Immunoassay Handbook - 4th Edition." https://www.elsevier.com/books/the-immunoassay-handbook/wild/978-0-08-097037-0 (accessed Jul. 15, 2022).

[19] F. X. R. Sutandy, J. Qian, C.-S. Chen, and H. Zhu, "Overview of protein microarrays," *Curr. Protoc. Protein Sci.*, vol. Chapter 27, p. Unit 27.1, Apr. 2013, doi: 10.1002/0471140864.ps2701s72.

[20] K. Shah and P. Maghsoudlou, "Enzyme-linked immunosorbent assay (ELISA): the basics," *Br. J. Hosp. Med. Lond. Engl. 2005*, vol. 77, no. 7, pp. C98-101, Jul. 2016, doi: 10.12968/hmed.2016.77.7.C98.

[21] C.-L. Hsu, A. Sun, Y. Zhao, E. Aronoff-Spencer, and D. A. Hall, "A 16$\times$ 20 electrochemical CMOS biosensor array with in-pixel averaging using polar modulation," in *2018 IEEE Custom Integrated Circuits Conference (CICC)*, 2018, pp. 1–4.

[22] A. C. Sun, E. Alvarez-Fontecilla, A. G. Venkatesh, E. Aronoff-Spencer, and D. A. Hall, "High-Density Redox Amplified Coulostatic Discharge-Based Biosensor Array," *IEEE J. Solid-State Circuits*, vol. 53, no. 7, pp. 2054–2064, Jul. 2018, doi: 10.1109/JSSC.2018.2820705.

[23] H. Li, X. Liu, L. Li, X. Mu, R. Genov, and A. J. Mason, "CMOS electrochemical instrumentation for biosensor microsystems: A review," *Sensors*, vol. 17, no. 1, p. 74, 2016.

[24] K. A. White, G. Mulberry, and B. N. Kim, "Parallel 1024-ch Cyclic Voltammetry on Monolithic CMOS Electrochemical Detector Array," *IEEE Sens. J.*, vol. 20, no. 8, pp. 4395–4402, Apr. 2020, doi: 10.1109/JSEN.2019.2961809.

[25] P. S. Singh, "From Sensors to Systems: CMOS-Integrated Electrochemical Biosensors," *IEEE Access*, vol. 3, pp. 249–259, 2015, doi: 10.1109/ACCESS.2015.2410256.

[26] S.-Y. Lu *et al.*, "A Review of CMOS Electrochemical Readout Interface Designs for Biomedical Assays," *IEEE Sens. J.*, vol. 21, no. 11, pp. 12469–12483, Jun. 2021, doi: 10.1109/JSEN.2021.3056443.

[27] S. Hwang, C. N. LaFratta, V. Agarwal, X. Yu, D. R. Walt, and S. Sonkusale, "CMOS Microelectrode Array for Electrochemical Lab-on-a-Chip Applications," *IEEE Sens. J.*, vol. 9, no. 6, pp. 609–615, Jun. 2009, doi: 10.1109/JSEN.2009.2020193.

[28] X. Zhou, M. Sveiven, and D. A. Hall, "A CMOS Magnetoresistive Sensor Front-End With Mismatch-Tolerance and Sub-ppm Sensitivity for Magnetic Immunoassays," *IEEE Trans. Biomed. Circuits Syst.*, vol. 13, no. 6, pp. 1254–1263, Dec. 2019, doi: 10.1109/TBCAS.2019.2949725.

[29] X. Zhou *et al.*, "A 9.7-nT_{rms}, 704-ms Magnetic Biosensor Front-End for Detecting Magneto-Relaxation," *IEEE J. Solid-State Circuits*, vol. 56, no. 7, pp. 2171–2181, Jul. 2021, doi: 10.1109/JSSC.2020.3043669.

[30] D. A. Hall, R. S. Gaster, K. Makinwa, S. X. Wang, and B. Murmann, "A 256 pixel magnetoresistive biosensor microarray in 0.18μm CMOS," *IEEE J. Solid-State Circuits*, vol. 48, no. 5, pp. 1290–1301, May 2013, doi: 10.1109/JSSC.2013.2245058.

[31] D. Ying, C.-Y. Tseng, P.-W. Chen, Y.-H. Lo, and D. Hall, "A 30.3 fA/Hz Biosensing Current Front-End with 139 dB Cross-Scale Dynamic Range," *IEEE Trans. Biomed. Circuits Syst.*, pp. 1–1, 2021, doi: 10.1109/TBCAS.2021.3124197.

[32] D. A. Hall *et al.*, "16.1 A nanogap transducer array on 32nm CMOS for electrochemical DNA sequencing," in *2016 IEEE International Solid-State Circuits Conference (ISSCC)*, Jan. 2016, pp. 288–289. doi: 10.1109/ISSCC.2016.7418020.

[33] J. Musayev, Y. Adlgüzel, H. Külah, S. Eminoğlu, and T. Akln, "Label-Free DNA Detection Using a Charge Sensitive CMOS Microarray Sensor Chip," *IEEE Sens. J.*, vol. 14, no. 5, pp. 1608–1616, May 2014, doi: 10.1109/JSEN.2014.2301693.

[34] L. Keeble, N. Moser, J. Rodriguez-Manzano, and P. Georgiou, "ISFET-Based Sensing and Electric Field Actuation of DNA for On-Chip Detection: A Review," *IEEE Sens. J.*, vol. 20, no. 19, pp. 11044–11065, Oct. 2020, doi: 10.1109/JSEN.2020.2998168.

[35] A. Cornish-Bowden, "One hundred years of Michaelis–Menten kinetics," *Perspect. Sci.*, vol. 4, pp. 3–9, Mar. 2015, doi: 10.1016/j.pisc.2014.12.002.

[36] Y. Choi *et al.*, "Single-Molecule Lysozyme Dynamics Monitored by an Electronic Circuit," *Science*, vol. 335, no. 6066, pp. 319–324, Jan. 2012, doi: 10.1126/science.1214824.

[37] Y. Choi *et al.*, "Dissecting Single-Molecule Signal Transduction in Carbon Nanotube Circuits with Protein Engineering," *Nano Lett.*, vol. 13, no. 2, pp. 625–631, Feb. 2013, doi: 10.1021/nl304209p.

[38] T. J. Olsen *et al.*, "Electronic Measurements of Single-Molecule Processing by DNA Polymerase I (Klenow Fragment)," *J. Am. Chem. Soc.*, vol. 135, no. 21, pp. 7855–7860, May 2013.

[39] S. Sek, "Review: Peptides and proteins wired into the electrical circuits: an SPM-based approach," *Biopolymers*, vol. 100, no. 1, pp. 71–81, 2013, doi: 10.1002/bip.22148.

[40] B. Zhang, E. Ryan, X. Wang, W. Song, and S. Lindsay, "Electronic Transport in Molecular Wires of Precisely Controlled Length Built from Modular Proteins," *ACS Nano*, vol. 16, no. 1, pp. 1671–1680, Jan. 2022, doi: 10.1021/acsnano.1c10830.

[41] B. Zhang, W. Song, J. Brown, R. Nemanich, and S. Lindsay, "Electronic Conductance Resonance in Non-Redox-Active Proteins," *J. Am. Chem. Soc.*, vol. 142, no. 13, pp. 6432–6438, Apr. 2020, doi: 10.1021/jacs.0c01805.

[42] S. Lindsay, "Ubiquitous Electron Transport in Non-Electron Transfer Proteins," *Life*, vol. 10, no. 5, p. 72, May 2020, doi: 10.3390/life10050072.

[43] M. A. Miled and M. Sawan, "Dielectrophoresis-Based Integrated Lab-on-Chip for Nano and Micro-Particles Manipulation and Capacitive Detection," *IEEE Trans. Biomed. Circuits Syst.*, vol. 6, no. 2, pp. 120–132, Apr. 2012, doi: 10.1109/TBCAS.2012.2185844.

[44] S. Sorgenfrei, C. Chiu, M. Johnston, C. Nuckolls, and K. L. Shepard, "Debye Screening in Single-Molecule Carbon Nanotube Field-Effect Sensors," *Nano Lett.*, vol. 11, no. 9, pp. 3739–3743, Sep. 2011, doi: 10.1021/nl201781q.

[45] S. Tsuji *et al.*, "RNA aptamer binding to polyhistidine-tag," *Biochem. Biophys. Res. Commun.*, vol. 386, no. 1, pp. 227–231, Aug. 2009, doi: 10.1016/j.bbrc.2009.06.014.

[46] I. Sgouralis and S. Pressé, "An Introduction to Infinite HMMs for Single-Molecule Data Analysis," *Biophys. J.*, vol. 112, no. 10, pp. 2021–2029, May 2017, doi: 10.1016/j.bpj.2017.04.027.